Research Square

Preprints are preliminary reports that have not undergone peer review.
They should not be considered conclusive, used to inform clinical practice,
or referenced by the media as validated information.

A relaxation-rate-separated Smagorinsky model for large-eddy simulation

Haotian Luo
Jiangsu Ocean University
Zhao-Quan Wen
Jiangsu Ocean University
Hongming Zhang
Jiangsu Ocean University
Lanming Zhao
zhaolm@jou.edu.cn
Jiangsu Ocean University

Research Article

Keywords: large-eddy simulation, subgrid-scale model, multiple-relaxation-time, anisotropy, strain-rate topology

Posted Date: November 16th, 2026

DOI: https://doi.org/10.21203/rs.3.rs-11172285/v1

License: This work is licensed under a Creative Commons Attribution 4.0 International License.
Read Full License

Additional Declarations: No competing interests reported.

A relaxation-rate-separated Smagorinsky model for large-eddy simulation

Hao-Tian Luo[1], Zhao-Quan Wen[1], Hong-Ming Zhang[1], Lan-Ming Zhao[1*]

[1*]School of Environmental and Chemical Engineering, Jiangsu Ocean University, Lianyungang, 222005, Jiangsu, China.

*Corresponding author(s). E-mail(s): zhaolm@jou.edu.cn;

Abstract

Large-eddy simulation (LES) closures based on a scalar eddy viscosity act identically on every component of the deviatoric resolved strain rate, so that the modelled subgrid-scale (SGS) stress remains aligned with the strain and cannot reflect the local flow topology. This work presents a relaxation-rate-separated Smagorinsky model that reactivates the dormant separation of the diagonal and off-diagonal relaxation rates of the D3Q27 multiple-relaxation-time (MRT) collision operator through a single dimensionless ratio $\boldsymbol{r_d}$. This separation is translated into an algebraic anisotropy-correction factor $\boldsymbol{f_{aniso}}$ that multiplies the standard Smagorinsky eddy viscosity. The correction is governed by a strain-rate topology sensor $\boldsymbol{\alpha}$ that vanishes in pure shear and approaches unity in pure normal straining, and it is designed to reduce identically to the standard Smagorinsky model at $\boldsymbol{r_d = 1}$ while remaining regular over the admissible parameter range. The model thus introduces a single additional parameter without altering the well-posedness of the closure. It is validated on a plane jet and against periodic-hill reference data at two Reynolds numbers. In the plane jet the correction preserves the dominant free-shear mechanisms and modulates the local SGS dissipation without artificially inflating the subgrid contribution; in the periodic-hills case the reattachment length is non-monotonic in $\boldsymbol{r_d}$, being longest at intermediate values, while the resolved turbulence intensity in the smooth region is lowest at the same setting. The results indicate that a single physically interpretable parameter can introduce direction-dependent SGS dissipation while leaving the resolved mean flow essentially unchanged.

Keywords: large-eddy simulation, subgrid-scale model, multiple-relaxation-time, anisotropy, strain-rate topology

1 Introduction

Large-eddy simulation (LES) resolves the energy-containing scales of turbulent motion and models the unresolved subgrid scales (SGS) through a closure hypothesis. The standard Smagorinsky model [1] supplies a scalar eddy viscosity proportional to the local strain-rate magnitude. Despite its simplicity and reasonable performance in homogeneous isotropic turbulence, the Smagorinsky closure suffers from three well-documented shortcomings: the coefficient C_s must be tuned for each flow; the model is excessively dissipative in near-wall regions and fails to vanish in laminar flow; and, fundamentally, a scalar ν_t acts identically on every tensorial component of $\widetilde{S}_{ij}^d$, forcing the SGS stress to remain co-aligned with the resolved strain rate irrespective of the local flow topology [2, 3]. On anisotropic grids, the choice of the subgrid length Δ further compounds these difficulties [4].

A broad family of closures has been developed to address these limitations (Table 1). Beyond eddy-viscosity closures, deconvolution-based models approximately invert the filter operator at increased cost [5], while the anisotropic structure-function model of Shao et al. [6] links the SGS stress directly to the resolved-scale energy transfer. These approaches, however, either retain a scalar ν_t or introduce multiple case-dependent coefficients.

A common thread connects these models: each ultimately supplies a *scalar* eddy viscosity. The difference lies in *how* that scalar is computed, not in *whether* the SGS stress may depart from co-alignment with $\widetilde{S}_{ij}^d$. Even the structure-function model of Cui et al. [7], which accounts for anisotropic energy transfer in its derivation, acknowledges that "the eddy viscosity is assumed to be a scalar; hence, it is an isotropic model." The reverse energy cascade in the buffer layer further contradicts the purely dissipative premise of most closures [8]. No existing model provides a single, physically interpretable parameter that explicitly controls the directional distribution of the SGS stress without sacrificing the simplicity of the Smagorinsky framework.

Three strands of recent work illustrate both the persistence of this limitation and its consequences. First, when an SGS model is coupled to a high-order discretisation, part of the dissipation is supplied by the numerical scheme itself, and the closure must be designed against that baseline rather than in isolation; Manzanero et al. [9] constructed a Smagorinsky spectral vanishing viscosity model for discontinuous Galerkin discretisations precisely by analysing the numerical dissipation of the scheme first. Second, the practical value of an SGS closure is increasingly judged on wall-bounded separated and bluff-body flows rather than on homogeneous turbulence, where the strain-rate topology is non-uniform: implicit LES of a square cylinder at $Re = 22{,}000$ [10] and large-eddy simulation of a hydrokinetic-turbine wake [11] both report strongly anisotropic Reynolds stresses that a scalar ν_t cannot represent by construction. Third, improvements to established closures are now typically validated against a hierarchy of canonical flows rather than a single case, as in the recent reassessment of the Baldwin–Lomax model [12]. The performance of any new closure therefore depends on the local strain topology, and a model that ignores it will be judged on flows where that dependence is strongest.

The present work explores a different route. Rather than refining the functional dependence of ν_t on the resolved field, we introduce a direction-dependent correction whose origin lies in the architecture of the multi-relaxation-time (MRT) collision operator of the lattice Boltzmann method. The theoretical advantages of MRT over single-relaxation-time (BGK) operators — improved stability and independent control of individual physical modes — were established by Lallemand and Luo [13]. In the D3Q27 MRT framework [14], five shear moments are relaxed independently: three off-diagonal moments at a rate s_{off} and two diagonal moments at a rate s_{diag}. The standard parameterization sets $s_{\text{diag}} = s_{\text{off}}$, a choice that maximises numerical stability but discards a structural degree of freedom absent in BGK. The D3Q27 lattice is preferred over D3Q19 because it preserves full rotational invariance of the stress tensor [15]. The combination of MRT collision with SGS closures has been demonstrated for temporal deconvolution by Simonis et al. [16], confirming that the MRT architecture can productively interface with turbulence modelling.

We activate the dormant separation of shear relaxation rates through a single ratio $r_d \equiv s_{\text{diag}}/s_{\text{off}}$, and translate its physical consequence into an algebraic correction factor $f_{\text{aniso}}(\alpha; r_d)$ that multiplies the Smagorinsky eddy viscosity. The sensor $\alpha = [(S^d_{xx})^2 + (S^d_{yy})^2 + (S^d_{zz})^2]/(S^d_{kl}S^d_{kl})$ characterises the local strain-rate topology: it vanishes in pure shear and approaches unity in pure normal straining. An isotropic reference value $\alpha_{\text{ref}} = 2/5$ follows rigorously from the isotropic tensor identity [17] and serves as the pivot about which the correction is applied. The functional form of f_{aniso} satisfies four design constraints: it reduces to unity at $\alpha = \alpha_{\text{ref}}$, degenerates identically to the standard Smagorinsky model at $r_d = 1$, is monotonic in α, and remains regular over the admissible parameter range.

The model has been implemented in OpenFOAM as a compressible LES eddy-viscosity closure. The correction is purely local and adds no inter-process communication, so it preserves the parallel scaling of the host solver. Section 2 presents the mathematical formulation, tracing the chain from MRT relaxation to the final eddy-viscosity expression. Section 3 describes the validation strategy and benchmark cases. Conclusions are drawn in Section 4.

Table 1 Comparison of eddy-viscosity SGS models (WALE: wall-adapting local eddy viscosity; AMD: anisotropic minimum dissipation). Here the strain-rate magnitude is defined as $|\mathbf{S}| = (2S_{ij}S_{ij})^{1/2}$

Model	Core expression	Anisotropy handling	Key limitation
Smagorinsky [1]	$\nu_t = (C_s\Delta)^2\lvert\widetilde{\mathbf{S}}^d\rvert$	None; scalar ν_t	Constant C_s; over-dissipative near walls
Dynamic Smagorinsky [18]	$C_s^2 = \langle L_{ij}M_{ij}\rangle / \langle M_{kl}M_{kl}\rangle$	Implicit via local $C_s(\mathbf{x},t)$; ν_t remains scalar	Averaging and clipping required
WALE [19]	$\nu_t = (C_w\Delta)^2\,(\widetilde{\mathbf{S}}^d : \widetilde{\mathbf{S}}^d)^{3/2} / \left[(\widetilde{\mathbf{S}} : \widetilde{\mathbf{S}})^{5/2} + (\widetilde{\mathbf{S}}^d : \widetilde{\mathbf{S}}^d)^{5/4}\right]$	Near-wall ν_t decay; scalar ν_t	Wall-only; no bulk anisotropy
Vreman [20]	$\nu_t = C\sqrt{B_\beta / \alpha_{ij}\alpha_{ij}}$	Switches off for specific $\nabla\mathbf{u}$; scalar ν_t	Backscatter dissipation
AMD [21]	$\nu_t = C\,\max\{-\lvert(\hat{\boldsymbol{\delta}}\cdot\nabla)\mathbf{u}\rvert^2, 0\} / \lvert\nabla\mathbf{u}\rvert^2$	Filter-width scaling for anisotropic grids; scalar ν_t	Frame-invariance correction [22]
Structure-function [7]	$\nu_t = C_{\mathrm{sf}}\,\Delta^2\,\lvert\widetilde{\mathbf{S}}^d\rvert\,\mathcal{F}(\delta u, \Delta)$	Anisotropic energy transfer in coefficient; ν_t scalar	Homogeneous turbulence
Mixed model [23]	$\tau_{ij}^{\mathrm{sgs}} = -2\nu_t\widetilde{S}_{ij}^d + C_{\mathrm{nl}}T_{ij}$	Reverse energy flux	Channel-flow-specific
Present	$\nu_t = (C_s\Delta)^2\lvert\widetilde{\mathbf{S}}^d\rvert\,\dfrac{1+\alpha\,\hat{\delta}}{1+0.4\,\hat{\delta}}$	Explicit, single-parameter r_d	Requires r_d calibration

2 Methodology

The approach begins from an architectural feature of the D3Q27 multi-relaxation-time (MRT) collision operator [14]: five shear moments are relaxed independently, yet the standard parameterization assigns them a common rate. We examine the consequence of lifting this constraint through a user-specified ratio $r_d \equiv s_{\mathrm{diag}}/s_{\mathrm{off}}$ between the diagonal and off-diagonal relaxation rates (Sec. 2.1). The physical effect — a direction-dependent subgrid-scale stress response — is translated into the finite-volume framework via a scalar sensor $\alpha = [(S^d_{xx})^2 + (S^d_{yy})^2 + (S^d_{zz})^2]/(S^d_{kl}S^d_{kl})$ that classifies the local strain-rate topology. An isotropic reference value $\alpha_{\mathrm{ref}} = 2/5$ is obtained from the isotropic tensor identity and serves as the pivot about which the correction is applied (Sec. 2.2). The correction takes the form of an algebraic factor $f_{\mathrm{aniso}}(\alpha; r_d) = (1+\alpha\hat{\delta})/(1+\alpha_{\mathrm{ref}}\hat{\delta})$ with $\hat{\delta} = 1/r_d - 1$, which multiplies the Smagorinsky eddy viscosity (Sec. 2.3). The design ensures $f_{\mathrm{aniso}}(\alpha_{\mathrm{ref}}) = 1$ for all r_d, so that isotropic turbulence is left unmodified, and at $r_d = 1$ the model reduces identically to the standard Smagorinsky closure (Sec. 2.4). The model is implemented as a compressible LES eddy-viscosity model in the open-source computational fluid dynamics (CFD) software OpenFOAM with six user-specified parameters (Sec. 2.5).

2.1 Separation of relaxation rates

The D3Q27 MRT collision operator relaxes independent linear combinations of the distribution function f_α at distinct rates:

$$m^*_k = m_k - s_k(m_k - m^{\mathrm{eq}}_k), \tag{1}$$

where $m_k = M_{k\alpha} f_\alpha$ and $s_k \in (0, 2)$. Among the 27 moments, the five controlling the deviatoric stress separate into two groups:

$$\begin{aligned} \text{Off-diagonal shear:} &\quad m_{xy},\ m_{yz},\ m_{xz} \ \longleftrightarrow\ s_{\mathrm{off}}, \\ \text{Diagonal shear:} &\quad m_{xx-yy},\ m_{xx+yy-2zz} \ \longleftrightarrow\ s_{\mathrm{diag}}. \end{aligned} \tag{2}$$

The off-diagonal group contributes to τ_{xy}, τ_{yz}, and τ_{xz}; the diagonal group to the normal-stress differences $\tau_{xx} - \tau_{yy}$ and $\tau_{xx} + \tau_{yy} - 2\tau_{zz}$.

The standard D3Q27 parameterization [14] adopts $s_{\mathrm{diag}} = s_{\mathrm{off}}$, so that all five moments relax at the same rate. This is a natural choice for numerical stability in LBM, but it discards a capability that has no analogue in the single-relaxation-time (BGK) operator. In the Gram–Schmidt orthonormalised D3Q27 Hermite basis the energy mode and the two diagonal shear modes span mutually orthogonal subspaces, so that the two relaxation rates are independent degrees of freedom: the architecture provides them, while the standard parameterization sets them equal and thereby leaves the capability unused. Anisotropy between the diagonal and off-diagonal shear channels is therefore a deliberate modelling choice rather than an inherited property of the collision operator, and the present model exercises it through r_d.

We introduce a single parameter to quantify the separation:

$$r_d \equiv \frac{s_{\mathrm{diag}}}{s_{\mathrm{off}}}, \tag{3}$$

which condenses two independent MRT rates into one ratio. A value $r_d \neq 1$ corresponds to $s_{\mathrm{diag}} \neq s_{\mathrm{off}}$ and implies a direction-dependent SGS stress response. In the following, this architectural capability is translated into a scalar eddy-viscosity correction suitable for a finite-volume LES solver.

2.2 A strain-rate topology indicator

To determine where the correction should act, a local indicator of the strain-rate topology is needed. The deviatoric strain-rate tensor $S^d_{ij} = \frac{1}{2}(\partial_j u_i + \partial_i u_j) - \frac{1}{3}\partial_k u_k \delta_{ij}$ encodes this information in the relative magnitudes of its diagonal and off-diagonal components. Consider the ratio

$$\begin{aligned} \alpha &= \frac{(S^d_{xx})^2 + (S^d_{yy})^2 + (S^d_{zz})^2}{S^d_{kl} S^d_{kl}} \\ &= \frac{(S^d_{xx})^2 + (S^d_{yy})^2 + (S^d_{zz})^2}{(S^d_{xx})^2 + (S^d_{yy})^2 + (S^d_{zz})^2 + 2[(S^d_{xy})^2 + (S^d_{yz})^2 + (S^d_{xz})^2]}, \end{aligned} \tag{4}$$

which satisfies $0 \leq \alpha \leq 1$. For simple shear $u_x(y)$, only $S^d_{xy} \neq 0$, giving $\alpha = 0$; for axisymmetric contraction, only the diagonal components are active, giving $\alpha = 1$. Intermediate values correspond to mixed topologies, and α is independent of the strain-rate magnitude $(2S^d_{kl}S^d_{kl})^{1/2}$.

A natural normalisation point is the value of α expected in isotropic turbulence. This follows from the isotropic tensor identity for three-dimensional traceless symmetric tensors [3, 17]:

$$\langle S_{ij} S_{kl} \rangle = A\delta_{ij}\delta_{kl} + B(\delta_{ik}\delta_{jl} + \delta_{il}\delta_{jk}), \tag{5}$$

where $\langle \cdot \rangle$ denotes an ensemble average over all orientations. The tracelessness condition $S_{ii} = 0$ imposes $3A + 2B = 0$, hence $A = -2B/3$. The component variances are

$$\begin{aligned} \langle (S^d_{xx})^2 \rangle = \langle (S^d_{yy})^2 \rangle = \langle (S^d_{zz})^2 \rangle = \tfrac{4}{3}B, \\ \langle (S^d_{xy})^2 \rangle = \langle (S^d_{yz})^2 \rangle = \langle (S^d_{xz})^2 \rangle = B, \end{aligned} \tag{6}$$

so that $\langle (S^d_{xx})^2 + (S^d_{yy})^2 + (S^d_{zz})^2 \rangle = 4B$ and $\langle S^d_{kl} S^d_{kl} \rangle = 10B$, yielding

$$\alpha_{\mathrm{ref}} = \frac{4B}{10B} = \frac{2}{5} = 0.4. \tag{7}$$

Equation (7) is a derived constant, not an empirical parameter. It serves as the pivot about which the correction is applied: at $\alpha = \alpha_{\mathrm{ref}}$ the correction factor reduces to

unity for any choice of r_d, so that the mean eddy viscosity in isotropic turbulence is unchanged.

2.3 An anisotropy-modulated closure

Define the imbalance relative to the isotropic state as

$$\hat{\delta} \equiv \frac{1}{r_d} - 1 = \frac{s_{\text{off}}}{s_{\text{diag}}} - 1, \tag{8}$$

so that $\hat{\delta} = 0$ at $r_d = 1$, and $\hat{\delta} > 0$ when the diagonal moments relax more slowly ($r_d < 1$). An algebraic factor is introduced to modulate the eddy viscosity:

$$f_{\text{aniso}}(\alpha) = \frac{1 + \alpha\,\hat{\delta}}{1 + \alpha_{\text{ref}}\,\hat{\delta}}, \qquad \alpha_{\text{ref}} = \tfrac{2}{5}. \tag{9}$$

Equation (9) satisfies four elementary constraints: (C1) $f_{\text{aniso}}(\alpha_{\text{ref}}) = 1$ for all r_d, so that the isotropic state is unchanged; (C2) $\lim_{r_d \to 1} f_{\text{aniso}} = 1$ for every α, recovering the unmodified Smagorinsky viscosity; (C3) monotonicity in α for fixed r_d, with the correction increasing from shear-dominated to strain-dominated regions when $r_d < 1$; (C4) no singularity for $\alpha \in [0, 1]$ and $r_d > 0$.

When $r_d < 1$, diagonal moments relax more slowly than off-diagonal moments and accumulate greater non-equilibrium stress. In shear-dominated regions ($\alpha < \alpha_{\text{ref}}$), this excess diagonal stress is unrelated to the prevailing shear topology, so that $f_{\text{aniso}} < 1$ reduces ν_t to avoid contaminating the SGS stress. In normal-strain-dominated regions ($\alpha > \alpha_{\text{ref}}$), the diagonal channels carry the physically relevant stress and $f_{\text{aniso}} > 1$ increases ν_t. The case $r_d > 1$ reverses the sign of the correction.

The form of Eq. (9) fixes the response completely: the correction vanishes identically at isotropy, grows linearly in $\hat{\delta}$, and is monotone in α for fixed r_d, so the strength of the modulation is set by the local strain-rate state together with the single parameter r_d. Its role is to target the regions where the co-alignment assumption of the scalar eddy-viscosity hypothesis is least appropriate.

The behaviour of the correction in a wall-bounded shear flow is fixed by the same algebra. In a canonical turbulent boundary layer the near-wall region is shear-dominated ($\alpha \ll \alpha_{\text{ref}}$), so that $r_d < 1$ yields $f_{\text{aniso}} < 1$ and *decreases* the eddy viscosity relative to the standard Smagorinsky closure. This is the opposite of the near-wall damping that wall-resolved LES requires, so the isotropic setting $r_d = 1$ is the appropriate choice for attached boundary layers, and the correction is reserved for flows with complex strain-rate topology — impingement, separation, and strong streamline curvature — where its direction-dependent modulation compensates for deviations from the assumption of SGS stress co-alignment with the resolved strain rate.

Assembling the components leads to the eddy viscosity

$$\nu_t = (C_s\Delta)^2 (2 S^d_{kl} S^d_{kl})^{1/2}\, f_{\text{aniso}}(\alpha) \;+\; \nu_t^{\text{shock}}, \tag{10}$$

where the optional shock-capturing contribution

$$\nu_t^{\text{shock}} = C_{\text{shock}}\Delta^2 \, \max(-\partial_k u_k,\, 0)\, \frac{1}{2}\left[1 + \tanh\left(\frac{Ma - Ma_0}{\Delta Ma}\right)\right] \tag{11}$$

is decoupled from the anisotropy mechanism and vanishes when $C_{\text{shock}} = 0$.

2.4 Reduction to the standard Smagorinsky model

At $r_d = 1$, $\hat{\delta} = 0$ and therefore $f_{\text{aniso}} \equiv 1$, giving

$$\nu_t\big|_{r_d=1,\, C_{\text{shock}}=0} = (C_s\Delta)^2 (2S_{kl}^d S_{kl}^d)^{1/2}, \tag{12}$$

which is the standard Smagorinsky closure without approximation. The present model contains the Smagorinsky model as an exact subset of its parameter space; the default configuration therefore reproduces the baseline against which the anisotropy correction is assessed.

For small departures from isotropy ($|r_d - 1| \ll 1$), expanding Eq. (9) to first order in $\hat{\delta}$ gives

$$f_{\text{aniso}}(\alpha) = 1 + (\alpha - \alpha_{\text{ref}})\,\hat{\delta} + \mathcal{O}(\hat{\delta}^2), \tag{13}$$

so that

$$\nu_t \approx (C_s\Delta)^2 (2S_{kl}^d S_{kl}^d)^{1/2}\big[1 + (\alpha - \alpha_{\text{ref}})\,\hat{\delta}\big]. \tag{14}$$

The first-order correction is antisymmetric about α_{ref}: for $r_d < 1$ it decreases ν_t in shear-dominated regions ($\alpha < \alpha_{\text{ref}}$) and increases it in strain-dominated regions ($\alpha > \alpha_{\text{ref}}$). In isotropic turbulence, where $\langle\alpha\rangle = \alpha_{\text{ref}}$, the leading-order correction integrates to zero; the mean dissipation rate is unchanged at this order regardless of r_d.

2.5 Implementation notes

Two remarks on the implementation follow from the form of Eq. (10). Because the correction multiplies an existing scalar viscosity rather than adding a tensor contribution, it inherits the well-posedness of the underlying Smagorinsky closure and introduces no additional coupling to the discrete momentum operator; the anisotropy enters through the local value of α, which is a pointwise algebraic function of the resolved velocity gradient. This is the same construction principle used when a physical closure is superimposed on a numerical dissipation mechanism already present in the discretisation [9], and it is why the modification can be introduced on grids whose aspect ratio varies strongly without altering the discretisation itself. Anisotropic grid adaptation is the usual route to controlling resolution in the directions of strong flow gradients [24, 25]; the present model addresses the complementary question of the directional response of the closure on such grids, since α is a frame-invariant scalar and therefore independent of the cell aspect ratio.

The model has been implemented as a compressible LES eddy-viscosity model in the open-source CFD software OpenFOAM, inheriting from `LESeddyViscosity`. Equation (10) is evaluated in the `correctNut()` member function using the velocity

gradient from `fvc::grad(U)`; the filter width Δ is supplied by the run-time selectable LES delta model. The six user-specified parameters are C_s (default 0.16), r_d (default 1.0), the ratio of specific heats γ (default 1.4), and the shock-viscosity constants C_{shock}, Ma_0, and ΔMa; the coefficients C_k and C_e are inherited from the base class for the SGS kinetic energy diagnostic. At each write time, the diagnostic fields α, f_{aniso}, Ma, and k are output for post-processing. Setting $r_d = 1$ and $C_{\text{shock}} = 0$ reproduces the standard Smagorinsky model identically.

3 Validation

The validation is organized around canonical flows in which the dominant strain topology is known a priori and the sensitivity to the anisotropy parameter can be separated from numerical uncertainty. All simulations were run with the same solver and the same time-integration settings, so that the differences reported below are attributable to the closure alone; this single-solver design is the standard practice when a closure is assessed across a flow hierarchy [12]. Three cases are considered. Case A is a spatially developing plane jet, which provides a free-shear benchmark with two well-defined shear layers, downstream vortex pairing, and progressive transition toward self-similarity. Cases B and C are the flow over periodic hills at two bulk Reynolds numbers, providing a wall-bounded benchmark that combines separation, reattachment, and strong streamline curvature at different levels of turbulence intensity.

3.1 Plane jet

3.1.1 Physical effect of the correction on the shear layers

The way in which the correction alters the flow is read directly from the filtered momentum equation. Writing the SGS stress as $\tau_{ij}^{\mathrm{sgs}} \simeq -2\nu_t \widetilde{S}_{ij}^{d}$ and considering the streamwise component,

$$\frac{\partial\langle u\rangle}{\partial t} + \langle u_j\rangle\frac{\partial\langle u\rangle}{\partial x_j} = -\frac{1}{\rho}\frac{\partial\langle p\rangle}{\partial x} + \frac{\partial}{\partial x_j}\Big[(\nu+\nu_t)\frac{\partial\langle u\rangle}{\partial x_j}\Big] + \frac{\partial\nu_t}{\partial x_j}\frac{\partial\langle u\rangle}{\partial x_j}, \tag{15}$$

in which the last term is the one the correction controls, since it is the only term that responds to the spatial variation of ν_t rather than to ν_t itself. Substituting the first-order expansion Eq. (14) splits this term into its Smagorinsky and topology-dependent parts,

$$\frac{\partial\nu_t}{\partial x_j}\frac{\partial\langle u\rangle}{\partial x_j} = \underbrace{\frac{\partial\nu_t^{(0)}}{\partial x_j}\frac{\partial\langle u\rangle}{\partial x_j}}_{\text{Smagorinsky}} + \nu_t^{(0)}\hat{\delta}\,\frac{\partial\alpha}{\partial x_j}\frac{\partial\langle u\rangle}{\partial x_j} + \mathcal{O}(\hat{\delta}^2). \tag{16}$$

The added term is a production-like contribution whose sign is set by the correlation between the strain-gradient vector and the topology gradient. Because the topology sensor is built from the strain-rate tensor, that correlation is fixed by the local flow structure. In a free shear layer it has a definite sign: the strain rate peaks where the flow is most shear-like, so the sensor is minimal exactly where $|\partial_y\langle u\rangle|$ is maximal, and the product in Eq. (16) is negative. With $\hat{\delta} > 0$ ($r_d < 1$) the topology-dependent term therefore opposes the Smagorinsky term at the shear layer, and $f_{\mathrm{aniso}} < 1$ reduces the local eddy viscosity precisely where the SGS stress is largest.

The measured fields confirm this ordering. Ranking the points of each streamwise plane by $|\partial_y\langle u\rangle|$, the reduction $1 - f_{\mathrm{aniso}}$ is largest in the shear-layer decile, smaller in the jet core, and smallest in the quiescent free stream: at $r_d = 0.5$ the modelled eddy viscosity falls by 20% in the shear layer, 10% at the core, and 9% in the free stream. The correction is therefore graded rather than uniform, and it removes the greatest amount of modelled dissipation exactly where the SGS stress governs the roll-up and

pairing of the layer. This gradient is the reason a single value of r_d produces a spatially selective response, and it is a direct consequence of the sensor being evaluated on the resolved strain-rate tensor.

The effect on the flow follows from the reduction of the SGS momentum flux $\nu_t\,\partial_y\langle u\rangle$ in the layer. That flux is the model's representation of the cross-layer momentum exchange that drives the spreading of the jet, so weakening it in the shear-dominated region leaves the layer to grow under the resolved motion alone. The measured vorticity thickness $\delta_\omega = \Delta U/\max|\partial_y\langle u\rangle|$, evaluated on the time-averaged profiles, separates the four cases at every downstream station and on both grids. At $x/d = 8$ it takes the values $0.405d$, $0.355d$, $0.538d$, and $0.625d$ on the fine grid for $r_d = 0.5$, 0.7, 0.9, and 1.0, and the coarser grid gives $0.300d$, $0.306d$, $0.360d$, and $0.422d$. The layer is thinner than the Smagorinsky value for every $r_d < 1$, by between 14% and 43% at this station, and the thinnest layer occurs at an intermediate setting ($r_d = 0.7$ on the fine grid and $r_d = 0.5$ on the coarser grid) rather than at the smallest r_d tested. The thickness is the quantity through which every downstream consequence of the correction is expressed, and its non-monotonic response mirrors the behaviour found below for the separated shear layer.

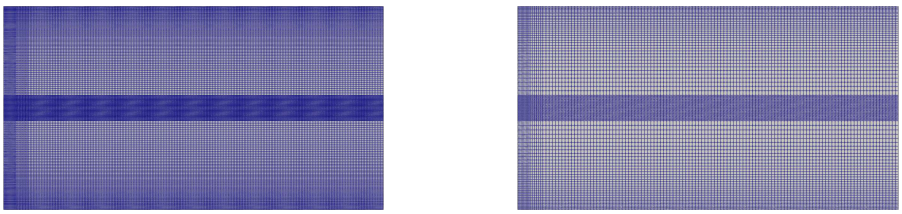
A thinner layer preserves the potential core of the jet over a longer streamwise distance. The time-averaged centerline velocity at $x/d = 12$ is 0.930 for $r_d = 0.5$ against 0.706 for $r_d = 1.0$ on the fine grid, and the instantaneous fields show the two shear layers remaining identifiable to a correspondingly larger x/d. The centerline fluctuation at the same station is correspondingly lower: it is 0.186 in absolute terms and 0.2213 when normalised by the local velocity difference Δu_c, against 0.325 and 0.5280 for $r_d = 1.0$. The reduced cross-layer exchange therefore concentrates the resolved motion in a thinner band and leaves the centreline correspondingly quieter, so that the response of the jet to r_d is governed by a single geometric quantity, the thickness of the layer in which the correction acts.

The modelled SGS kinetic energy provides an independent check that the correction does not act as an energy sink. Between the coarser and finer grids it drops from 1.112 to 0.267 at $x/d = 8$ for $r_d = 0.5$, so the modelled contribution shrinks as the cutoff wavenumber is raised and the resolved field carries the corresponding motion.

3.1.2 Numerical setup

The plane-jet configuration is that of the benchmark used by Sun et al. [26], which in turn is based on the LES and DNS studies of Le Ribault et al. [27] and Stanley et al. [28]. The computational domain is $30d \times 16d \times 4d$, with the jet centered at $y/d = 8$ and periodic boundary conditions in the spanwise direction. The inlet velocity is a smooth top-hat profile with $u_{jet} = 1$, $u_{co} = 0.09$, $d = 1$, and $h = 0.05d$, so that the co-flow-to-jet velocity-difference ratio is close to that adopted in the reference plane-jet calculations. The jet Reynolds number is $Re_d = U_j d/\nu = 6.4 \times 10^4$. Two grids are considered to isolate the sensitivity of the anisotropy correction from grid-resolution effects. The coarser grid contains $128 \times 101 \times 16$ cells and is refined in the inlet shear-layer region, while the finer grid contains 1,654,784 cells, obtained by refining each direction by a factor of two in the streamwise, normal, and spanwise directions; the finer grid therefore contains eight times as many cells as the coarser grid, as shown in

Fig. 1. For each grid, four simulations were performed with $r_d = 0.5$, 0.7, 0.9, and 1.0, while all other model parameters were kept fixed at $C_s = 0.16$ and $C_{\text{shock}} = 0$. The statistical sampling used below starts after the initial transient; for $r_d = 0.5$, 0.7, and 0.9 the averaging interval is $100 \leq t \leq 200$, whereas the available $r_d = 1.0$ samples cover $120 \leq t \leq 200$.



(a) finer grid (b) coarser grid

Fig. 1 Computational grids used for the plane-jet validation, both refined in the inlet shear-layer region: (a) finer grid and (b) coarser grid

3.1.3 Computational results

Figure 2 shows the downstream evolution of the normalised streamwise velocity fluctuation along the jet centerline, $u_{\text{rms}}/\Delta u_c$, where $\Delta u_c = \langle u \rangle_c - u_{co}$. This normalisation follows the comparison used for the drift-velocity model and the DNS/experimental data in Refs. [26, 28, 29]. For each r_d the fine and coarser grids are shown together, so that the resolution dependence of the resolved fluctuation can be assessed separately from the anisotropy correction. All calculations preserve the low fluctuation level in the near field and the rapid growth after $x/d \simeq 9$, where the two shear layers interact more strongly. The finer grid systematically yields a higher resolved fluctuation level than the coarser grid, consistent with an increase in the resolved small-scale content as the cutoff wavenumber is raised. At $x/d = 12$ the fine-grid values reach 0.2213, 0.1790, 0.2389, and 0.5280 for $r_d = 0.5$, 0.7, 0.9, and 1.0, respectively, whereas the coarser-grid values are 0.1278, 0.1200, 0.1989, and 0.1375. The ordering with r_d and the contrasting resolution dependence of the $r_d = 1.0$ case show that the correction acts through the local strain topology rather than as a global damping coefficient: it changes the balance between shear-layer roll-up and downstream mixing according to where the strain is shear-dominated.

The instantaneous fields in Figs. 3 and 4 show the corresponding structural response for the fine and coarser grids at each r_d. The velocity-magnitude contours retain the two inlet shear layers, which then develop into smaller-scale structures after vortex pairing, consistent with the qualitative sequence reported by Sun et al. [26]. The vorticity-magnitude contours reveal the roll-up and pairing of the two shear layers, with the finer grid resolving additional small-scale vortical activity. Both the resolved velocity and vorticity fields therefore become increasingly resolved on the finer grid, while the qualitative arrangement of the two shear layers remains unchanged. This

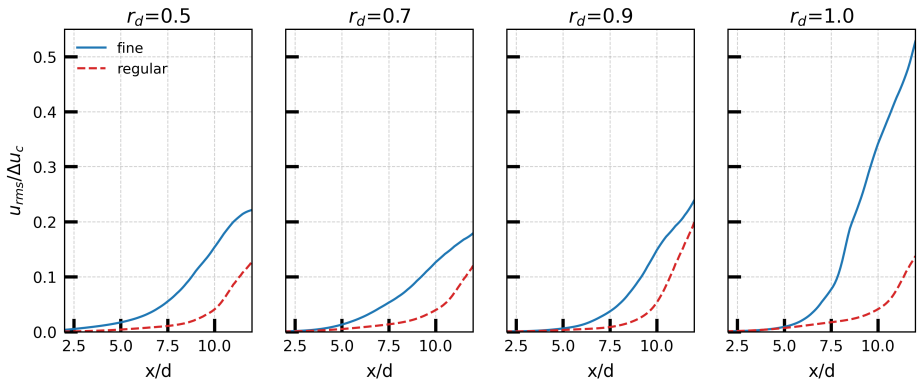


Fig. 2 Downstream evolution of the normalised longitudinal velocity fluctuations along the plane-jet centerline for the fine and reference grids at each r_d

supports the intended use of the model: r_d modulates where and how much SGS dissipation is applied in the shear layers, whereas the centerline fluctuation in Fig. 2 reflects the integrated downstream consequence of that local modulation.

Profiles at $x/d = 3$, 5, and 8 are shown in Fig. 5 for each r_d. Following the diagnostics introduced in Ref. [26], each panel reports the resolved partial-average fluctuation proxy $\tilde{u}_{PA}/u_{jet} = \langle \max(u - \langle u \rangle, 0) \rangle / u_{jet}$ and the normalised SGS kinetic energy $k_{sgs}/k_{sgs,jet}$; the mean streamwise velocity is omitted for clarity. The proxy is evaluated directly from the resolved velocity field and provides the same bimodal signature as the drift-velocity diagnostic of Ref. [26]. Both diagnostics exhibit that bimodal form, with peaks collocated with the two mean-velocity gradients. At $x/d = 8$, the fine-grid proxy reaches 0.0985, 0.0842, 0.1040, and 0.1552 for $r_d = 0.5$, 0.7, 0.9, and 1.0, respectively, while the corresponding coarser-grid values are 0.1085, 0.0850, 0.1253, and 0.1508. The proxy is therefore only weakly dependent on the grid resolution, whereas the normalised SGS kinetic energy is much more sensitive: at the same station the fine-grid $k_{sgs}/k_{sgs,jet}$ peaks are 0.267, 0.287, 0.293, and 0.162, against 1.112, 1.082, 0.986, and 0.775 on the coarser grid. The much lower modelled kinetic energy on the finer grid is consistent with a transfer of activity from modelled to resolved scales as the cutoff wavenumber is raised. This is the behaviour required of a closure that is added to, rather than substituted for, the numerical dissipation of the discretisation [9]: the modelled contribution shrinks as the grid supplies more of the dissipation directly.

The action of the correction is governed by the local strain-rate topology. For each r_d, Fig. 6(a) shows the correction factor f_{aniso} as a function of the topology indicator α. All four curves intersect at $\alpha = \alpha_{\text{ref}} = 2/5$, where the correction leaves the eddy viscosity unchanged, and f_{aniso} decreases monotonically toward $\alpha = 0$ (pure shear) and increases toward $\alpha \to 1$ (pure normal strain). As r_d departs from unity the correction is amplified, whereas $r_d = 1.0$ recovers the standard Smagorinsky closure with $f_{\text{aniso}} \equiv 1$ for all α. The probability density function of α in the developing jet is shown in Fig. 6(b); it is bimodal, peaked near $\alpha \approx 0$ in the shear layers, where the strain is shear-dominated, and near $\alpha \to 1$ at the jet core, so that the correction acts predominantly in these two topologically distinct regions.

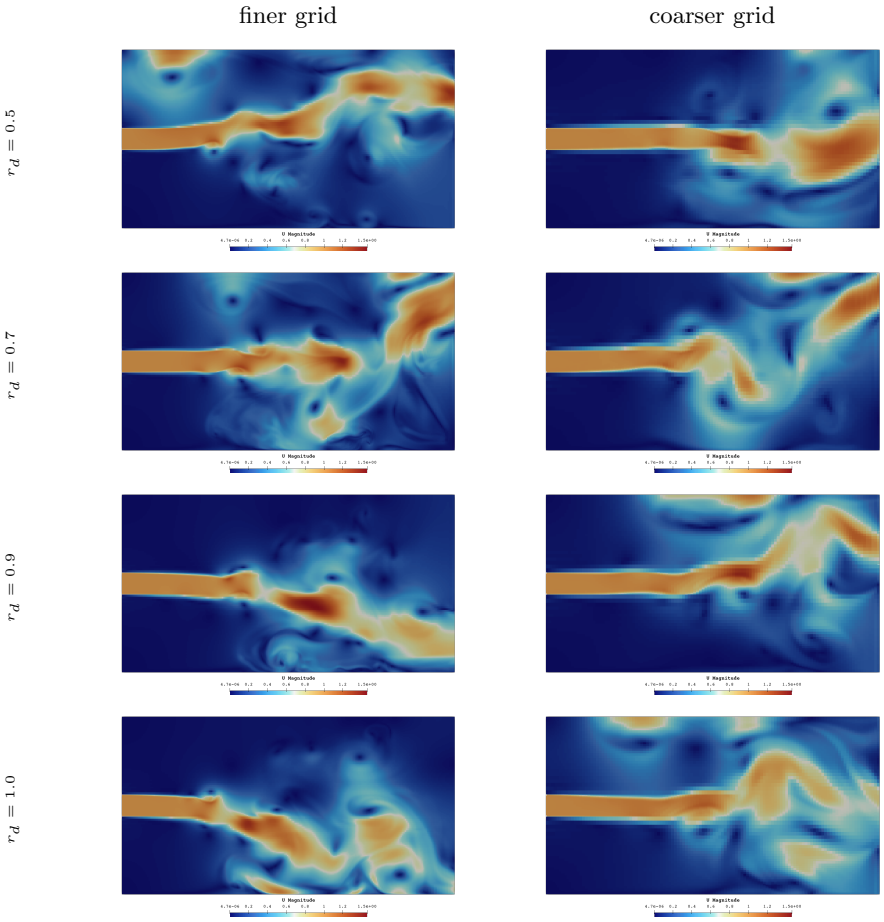


Fig. 3 Instantaneous velocity-magnitude contours in the plane-jet mid-plane on the finer (left column) and coarser (right column) grids at each r_d

Overall, the plane-jet validation shows that the correction preserves the main free-shear mechanisms of the reference studies: two-layer roll-up, downstream vortex breakdown, bimodal fluctuation and SGS-energy profiles, and centerline fluctuation growth. The resolution study confirms that the modelled-to-resolved energy transfer increases with grid resolution, and that r_d modulates the local SGS dissipation without artificially inflating the subgrid contribution. Among the tested values, $r_d = 0.7$ gives the lowest downstream fluctuation level and $r_d = 0.9$ the highest of the modulated cases, so the setting that most strongly damps the cross-layer exchange also produces the quietest jet. The case is therefore useful for calibrating free-shear behaviour. The response is governed by the bimodal topology of the free shear layer, which is the topic of the following subsection.

Two aspects of this case fix the interpretation of the model. First, the bimodal distribution of the topology indicator α (Fig. 6b) is the direct consequence of the two competing strain topologies that coexist in a free-shear flow: the nearly isotropic core of

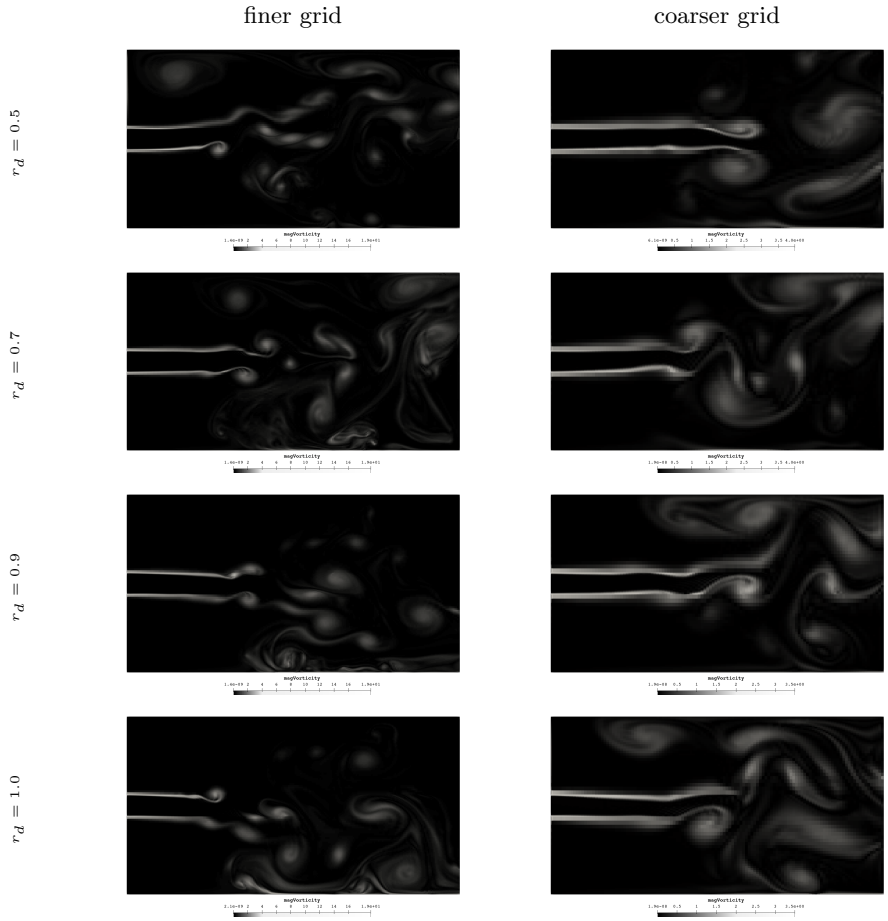


Fig. 4 Instantaneous vorticity-magnitude contours in the plane-jet mid-plane on the finer (left column) and coarser (right column) grids at each r_d

the jet, where the strain is dominated by normal deformation, and the two shear layers flanking it, where the strain is dominated by shear. The bimodality is what makes the correction spatially graded rather than uniform: because f_{aniso} varies with α, the two populations of cells receive different modulation strengths, and the response of the jet is set by the relative weight of the two modes rather than by a single dissipation level. Second, the fact that the modelled SGS kinetic energy is much lower on the finer grid (e.g. $k_{sgs}/k_{sgs,jet} = 0.267$ against 1.112 at $x/d = 8$ for $r_d = 0.5$) confirms that the anisotropy correction does not introduce an artificial sink of resolved energy as the resolution is refined, which is a key requirement for a model that is intended to sit alongside, rather than replace, the resolved turbulent motion.

3.2 Effect of the correction on the separated shear layer

The separated flow over a periodic hill isolates the second regime in which the correction operates. In the recirculation region the mean velocity gradient is carried almost

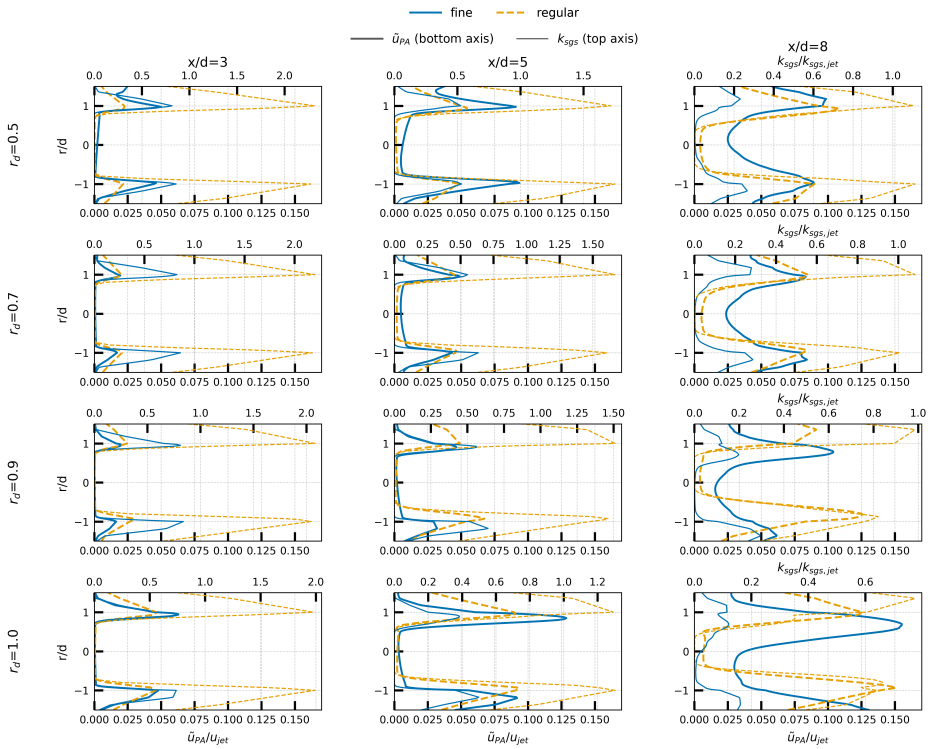
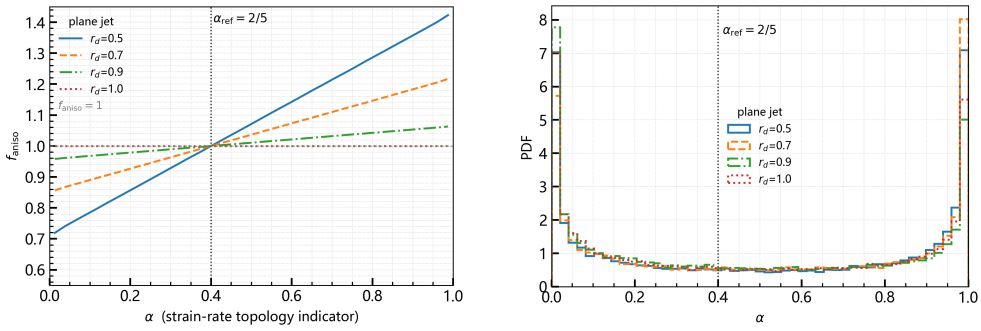


Fig. 5 Resolved partial-average fluctuation proxy (bottom axis, $\tilde{u}_{PA}/u_{jet}$) and normalised SGS kinetic energy (top axis, $k_{sgs}/k_{sgs,jet}$) versus r/d at three stations $x/d = 3$, 5, and 8 (columns) for the fine (solid) and reference (dashed) grids at each r_d (rows)



(a) (b)

Fig. 6 Anisotropy of the proposed closure for the plane-jet case at each r_d. (a) Correction factor f_{aniso} versus the strain-rate topology indicator α; the vertical dashed line marks the isotropic reference value $\alpha_{\text{ref}} = 2/5$, where $f_{\text{aniso}} = 1$ for all r_d. (b) Probability density function of α; the distribution is bimodal, peaked in the shear layers ($\alpha \approx 0$), where the strain is shear-dominated, and at the jet core ($\alpha \to 1$)

entirely by a single off-diagonal component, $\partial u/\partial y$, so that the resolved strain-rate tensor reduces to

$$\widetilde{S}_{ij} \simeq \begin{pmatrix} 0 & \frac{1}{2}\,\partial_y\langle u\rangle & 0 \\ \frac{1}{2}\,\partial_y\langle u\rangle & 0 & 0 \\ 0 & 0 & 0 \end{pmatrix}, \qquad \alpha = \frac{(S^d_{xx})^2 + (S^d_{yy})^2 + (S^d_{zz})^2}{S^d_{kl}S^d_{kl}} \longrightarrow 0. \tag{17}$$

The sensor therefore moves toward the shear end of its range, and it does so as a consequence of the mean strain tensor rather than of the turbulence intensity. The measured field bears this out: the recirculation region is strongly shear-dominated in the sense of the sensor, and the value it takes is essentially the same at $Re_b = 5600$ and 10600. Since the indicator is fixed by the geometry of the separation, the response of the closure is set by the mean flow rather than by the turbulence intensity.

Substituting Eq. (17) into the closure gives the eddy viscosity carried by the separated layer,

$$\nu_t \simeq (C_s\Delta)^2\,\big|\partial_y\langle u\rangle\big|\Big[1 + (\langle\alpha\rangle - \alpha_{\mathrm{ref}})\,\hat{\delta}\Big], \tag{18}$$

so that the SGS exchange across the layer is scaled by the bracket. Since the recirculation region is shear-dominated, the bracket falls below unity for every $r_d < 1$, and it decreases monotonically as r_d departs from one, relative to the standard Smagorinsky value ν_t^{SM}:

$$\frac{\nu_t}{\nu_t^{\mathrm{SM}}} = 1 + (\alpha_{\mathrm{rec}} - \alpha_{\mathrm{ref}})\Big(\frac{1}{r_d} - 1\Big) < 1 \qquad \text{for all } r_d < 1, \tag{19}$$

where α_{rec} denotes the indicator averaged over the recirculation region. Averaging the modelled viscosity over the cells with $\langle u_x\rangle < 0$ recovers this behaviour: the reduction is $\nu_t/\nu_t^{\mathrm{SM}} = 0.850$ at $r_d = 0.5$, 0.924 at $r_d = 0.7$, and 0.978 at $r_d = 0.9$, and it vanishes identically at $r_d = 1$.

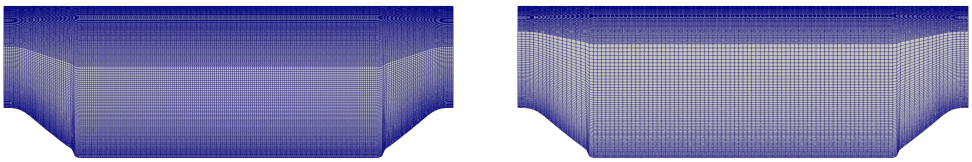
Because the reduction is largest where the modelled viscosity is largest, the scalar closure is weakened precisely in the layer that controls the separation. The dynamical consequence follows from the wall-normal momentum balance across that layer: writing the layer thickness as δ_s and the velocity difference across it as U_s, the SGS contribution to the momentum exchange is $\int \nu_t\,\partial_y\langle u\rangle\,\mathrm{d}y \sim \nu_t U_s/\delta_s$. Thinning this coupling reduces the entrainment that closes the bubble, so the recirculation is sustained further downstream and the reattachment point moves with r_d. The response is spatially selective: the isolation of the shear component in Eq. (17) is characteristic of the separated layer, whereas in the attached boundary layer over the hill crest and in the core channel flow the strain tensor retains its three-dimensional character and the sensor remains closer to α_{ref}. This is the distinguishing feature of the present closure relative to a change of C_s: the response is set by $(\langle\alpha\rangle - \alpha_{\mathrm{ref}})$, so it is spatially selective rather than uniform.

Two testable consequences follow from Eq. (18) and are examined in the results below. The correction acts through the product $(\langle\alpha\rangle - \alpha_{\mathrm{ref}})\hat{\delta}$, so the reattachment length must approach its Smagorinsky value continuously as $r_d \to 1$ from below. In addition, because $\langle\alpha\rangle$ is fixed by the geometry, the longest recirculation should occur

at the same r_d at both Reynolds numbers, while the absolute magnitude responds to the thinner separating layer at the higher Reynolds number.

3.3 Periodic hills: $Re_b = 5600$

Case B is the flow over periodic hills, a wall-bounded benchmark that combines separation, reattachment, and strong streamline curvature. Following the numerical and experimental studies of Breuer et al. [30] and the ERCOFTAC classic collection [31], the standard two-dimensional periodic-hill configuration is adopted without modification. The domain covers one hill period, with streamwise and spanwise lengths of $9h$ and $4.5h$ and a channel height of $3.035h$ measured from the flat floor to the upper wall, where h is the hill height. The lower wall follows the six-polynomial ERCOFTAC hill profile [30, 31]: the crest is located at $x/h = 0$, and by periodicity at $x/h = 9$, and the floor is flat for $1.929 \leq x/h \leq 7.071$. The bulk Reynolds number is formed with the hill height and the bulk velocity, $Re_b = U_b h/\nu$, and takes the values 5600 (case B) and 10600 (case C). The same two grids are used throughout, a fine grid and a coarser grid, as shown in Fig. 7; the coarser grid contains 997,248 cells and the finer grid contains 3,978,240 cells, obtained by refining each direction non-uniformly; the finer grid therefore contains four times as many cells as the coarser grid. Both grids resolve the hill profile in the near-wall region. Four simulations were performed on each grid with $r_d = 0.5$, 0.7, 0.9, and 1.0, while all other model parameters were kept fixed at $C_s = 0.16$ and $C_{\text{shock}} = 0$. The mean-flow statistics are accumulated over the interval $207 \leq t \leq 495$, corresponding to roughly 32 flow-through times after the initial transient.



(a) finer grid (b) coarser grid

Fig. 7 Computational grids used for the periodic-hills case, both resolving the hill profile in the near-wall region: (a) finer grid and (b) coarser grid

3.3.1 Resolved velocity magnitude

The instantaneous resolved velocity-magnitude field of the periodic-hills flow retains the qualitative structure of the benchmark: an accelerating stream over the hill crest, a large recirculation zone, and reattachment further downstream. The flow is populated by small-scale vortical structures that are advected along the separating shear layer and within the recirculation region, reflecting the resolved turbulent content that the anisotropy correction is intended to modulate. The large-scale arrangement of the

recirculation region remains unchanged by r_d, confirming that the correction does not alter the overall flow topology even as it redistributes the local SGS dissipation. The corresponding instantaneous velocity-magnitude contours on the finer and coarser grids at each r_d are provided in Fig. 8.

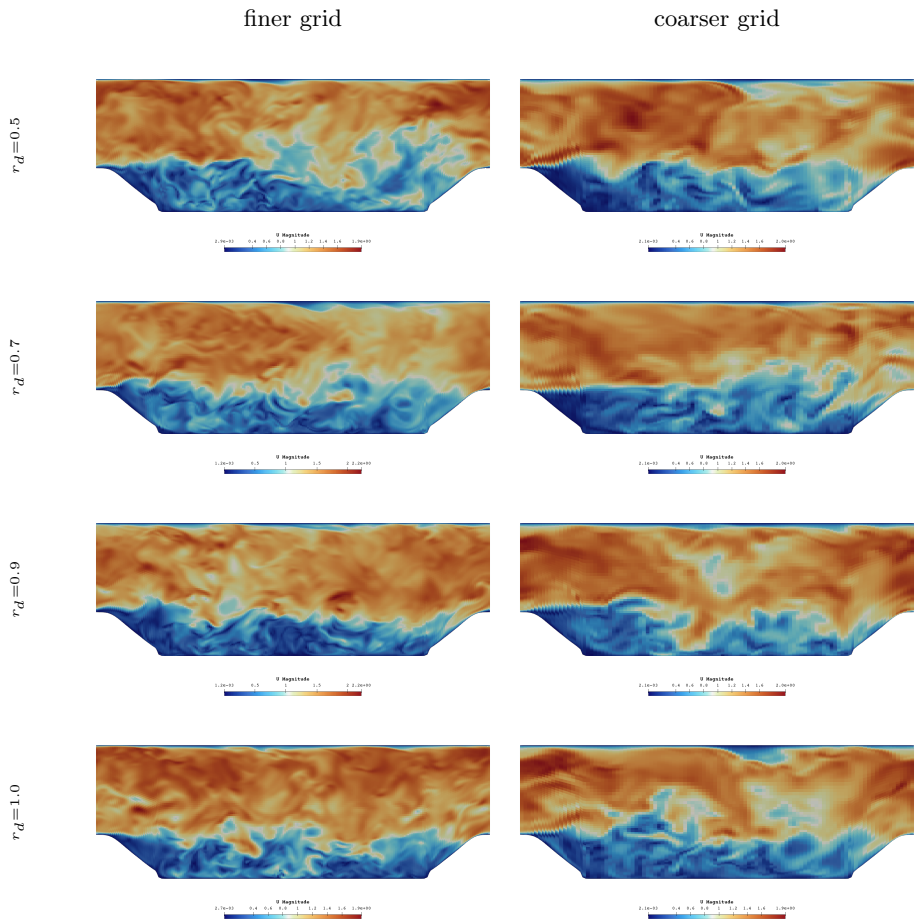


Fig. 8 Instantaneous resolved velocity-magnitude contours in the periodic-hills case at $Re_b = 5600$ on the finer (left column) and coarser (right column) grids at each r_d

3.3.2 Time-averaged streamwise velocity

The time-averaged streamwise velocity (Fig. 9) exhibits the same structure. The recirculation zone, identified by the region of reversed flow immediately behind the crest, is clearly resolved on the finer grid and is reproduced almost identically on the coarser grid. Its streamwise extent changes with r_d: it is shortest for $r_d = 1.0$ and longest for the intermediate values around $r_d = 0.7$.

The strength of the reversed flow, by contrast, is essentially independent of r_d. The region of reversed flow occupies 8.5–9.0% of the domain for all four values, and the minimum streamwise velocity lies between -0.38 and $-0.41\,U_b$ in every case, with a region-averaged value close to $-0.16\,U_b$. The anisotropy correction therefore modifies the streamwise extent of the separation bubble without altering the intensity of the reverse flow within it, which is consistent with a mechanism that acts on the local subgrid dissipation rather than on the mean momentum balance.

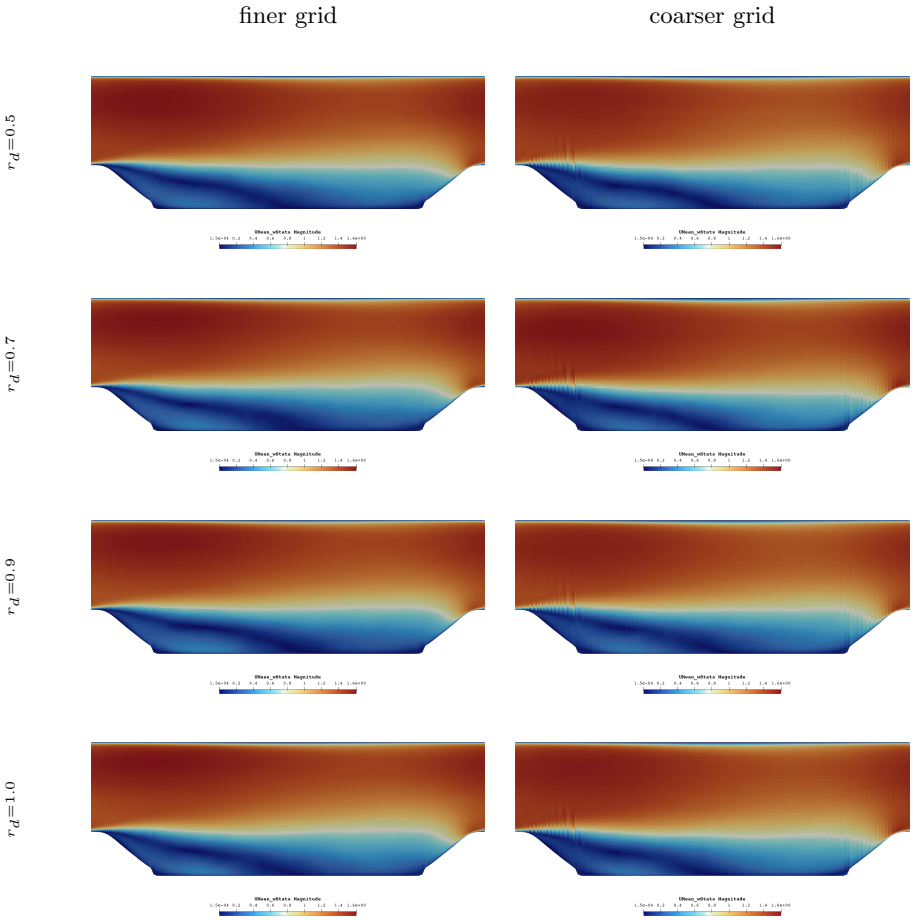


Fig. 9 Time-averaged streamwise velocity in the periodic-hills case at $Re_b = 5600$ on the finer (left column) and coarser (right column) grids at each r_d

3.3.3 SGS eddy viscosity

The SGS eddy viscosity (Fig. 10) is concentrated in a narrow band along the shear layer that separates from the hill crest and in the recirculation zone, where the strain

rate is largest. Its spatial distribution changes systematically with r_d, reflecting the direction-dependent modulation of the closure.

The mechanism is quantified by the topology indicator. Averaged over the cells of the reversed-flow region, the indicator is essentially independent of r_d and lies at the shear end of its range, below the isotropic pivot $\alpha_{\mathrm{ref}} = 2/5$. The recirculation region is therefore shear-dominated, and the correction with $r_d < 1$ yields $f_{\mathrm{aniso}} < 1$ there, reducing the modelled eddy viscosity below the standard Smagorinsky value. Because the mean indicator lies close to the pivot, the reduction is moderate rather than severe, and it grows monotonically as r_d departs from unity, in accordance with Eq. (9) at fixed α. At $r_d = 1.0$ the correction is identically unity, recovering the standard Smagorinsky viscosity exactly. The resulting reduction of the modelled viscosity in the shear-dominated recirculation region is the mechanism behind the longer separation bubble reported below.

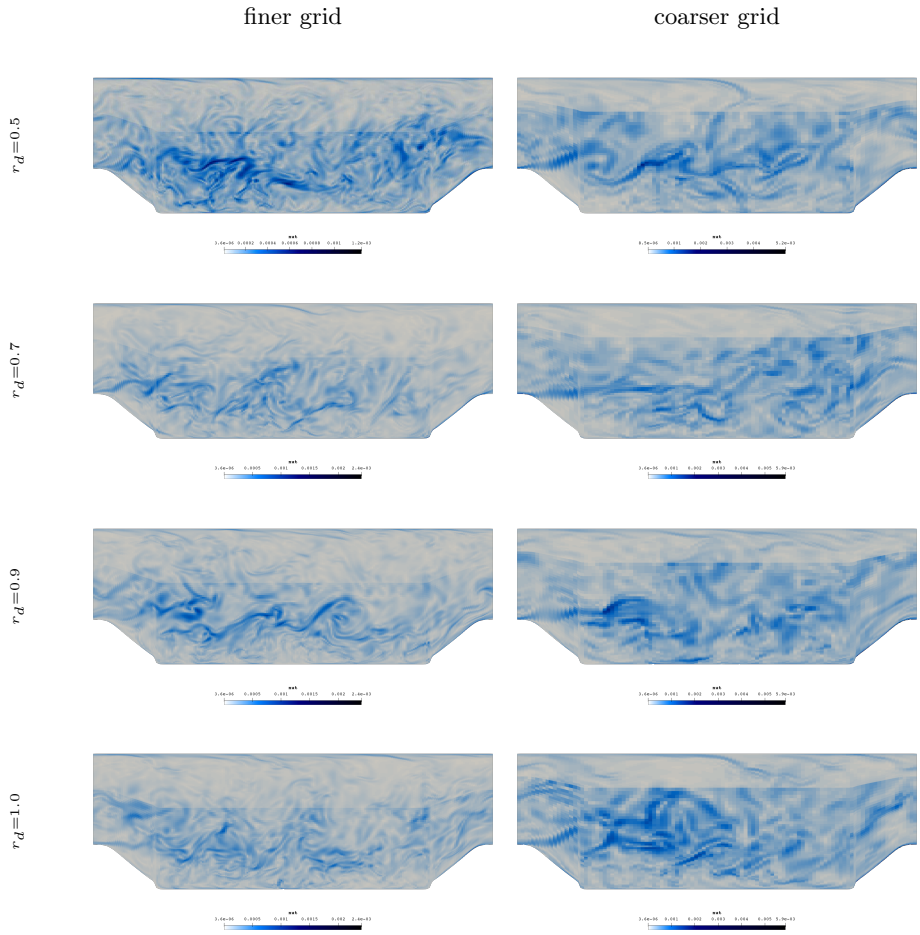


Fig. 10 SGS eddy viscosity in the periodic-hills case at $Re_b = 5600$ on the finer (left column) and coarser (right column) grids at each r_d

3.3.4 Profiles

The sampled profiles in Figs. 11–12 quantify the streamwise development of the mean velocity and the turbulence intensity at five stations behind the crest. At $x/h = 0.5$, within the recirculation region, the mean velocity is negative near the wall, reaching about $-0.15\,U_b$, and this region of reversed flow is somewhat deeper for the intermediate r_d values than for $r_d = 1.0$. Further downstream the boundary layer reattaches and recovers; by $x/h = 8$ the near-wall velocity is positive throughout. The fine and coarser-grid profiles nearly collapse onto each other, confirming that the present grid resolution is sufficient for the mean field.

The turbulence-intensity profiles show a pronounced peak in the shear layer that separates from the hill crest, with u_{rms} reaching $0.4\,U_b$ at $x/h = 0.5$. The intensity decays downstream as the shear layer relaxes, and the peak broadens and shifts away from the wall. In the smooth region above the recirculation zone ($x/h \geq 4$, $y/h \approx 1.5$–2.5) the four r_d values separate systematically, and the resolved fluctuation is smallest at $r_d = 0.7$. The response is therefore not monotone in the departure of r_d from unity: the quietest smooth region and the longest recirculation occur at the same intermediate setting, while the mean flow remains essentially unaffected.

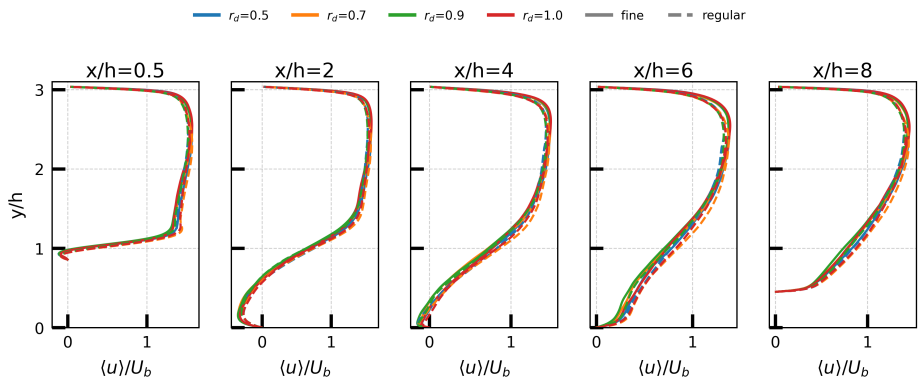


Fig. 11 Streamwise mean-velocity profiles $\langle u\rangle/U_b$ at five stations $x/h = 0.5, 2, 4, 6, 8$ for the periodic-hills case at $Re_b = 5600$ (case B) on the fine (solid) and coarser (dashed) grids at each r_d

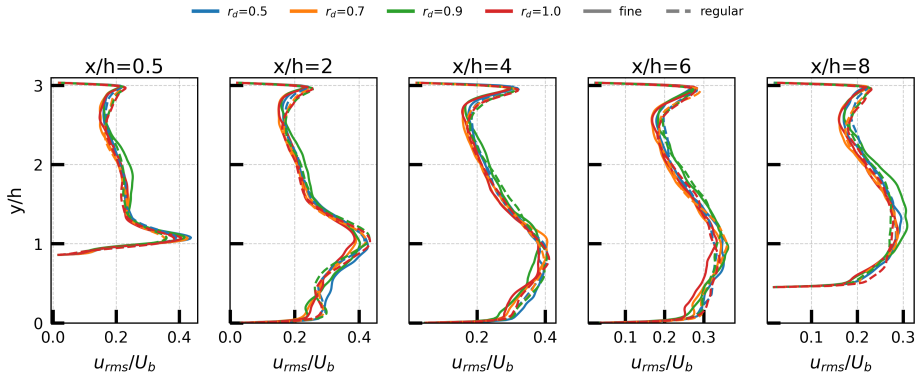


Fig. 12 Turbulence-intensity profiles u_{rms}/U_b at the same five stations for $Re_b = 5600$ (case B), fine (solid) and coarser (dashed) grids at each r_d

3.4 Periodic hills: $Re_b = 10600$

Case C uses the same domain, grids, and model parameters as case B, and differs only in the bulk Reynolds number, which is increased to $Re_b = 10600$. The same statistics interval and r_d values are retained, so that the case B and case C results are directly comparable.

3.4.1 Resolved velocity magnitude

The instantaneous resolved velocity-magnitude field at $Re_b = 10600$ shows the same qualitative recirculating structure as case B, but the higher Reynolds number produces a thinner separating shear layer and a stronger, more elongated recirculation bubble populated by smaller-scale vortical structures. As before, the overall flow topology is insensitive to r_d. The corresponding instantaneous velocity-magnitude contours on the finer and coarser grids at each r_d are provided in Fig. 13.

3.4.2 Time-averaged streamwise velocity

The time-averaged streamwise velocity (Fig. 14) again shows the recirculation zone immediately behind the crest. Its streamwise extent is largest for the intermediate r_d values and shortest for $r_d = 1.0$, mirroring the trend found in case B. The reversed-flow region occupies 8.2–8.7% of the domain across the four values, slightly smaller than at the lower Reynolds number, and the minimum streamwise velocity lies between -0.39 and $-0.41\,U_b$ with a region-averaged value of about $-0.16\,U_b$. As in case B, the intensity of the reversed flow is essentially unaffected by r_d, so that the correction changes the streamwise extent of the bubble while leaving the mean momentum distribution inside it intact.

3.4.3 SGS eddy viscosity

The SGS eddy viscosity (Fig. 15) is again concentrated along the separating shear layer and in the recirculation region. The topology statistics confirm the same mechanism

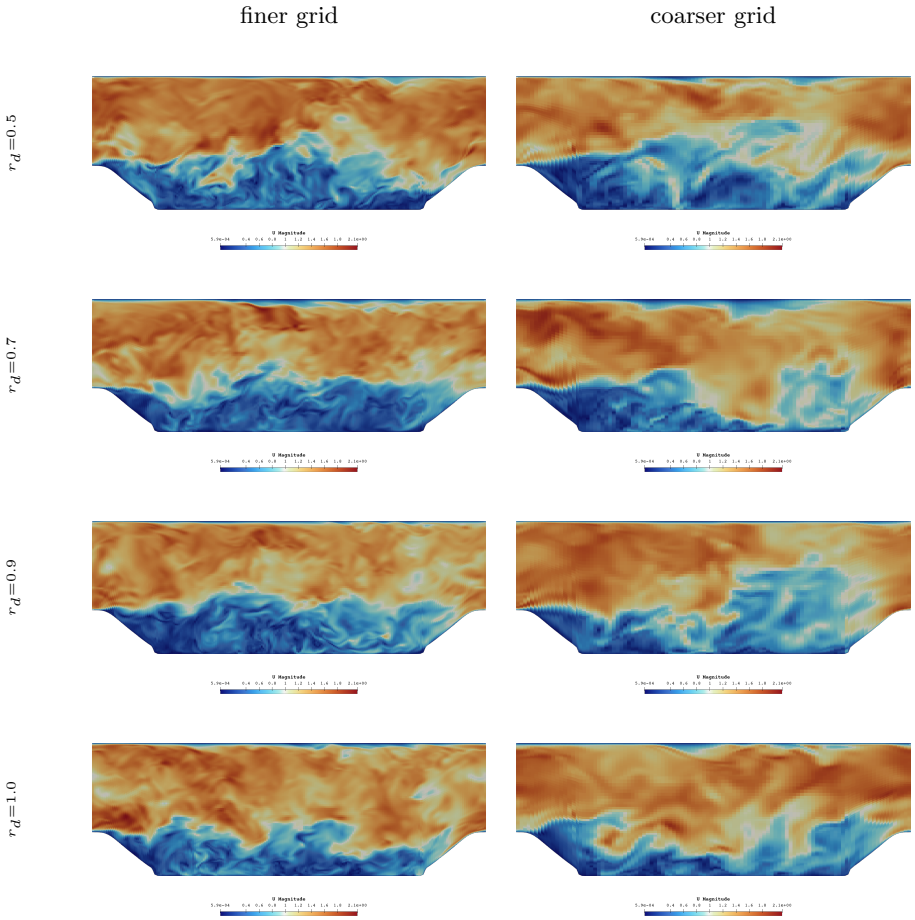


Fig. 13 Instantaneous resolved velocity-magnitude contours in the periodic-hills case at $Re_b = 10600$ on the finer (left column) and coarser (right column) grids at each r_d

as in case B: the region-averaged indicator is again independent of r_d and lies below α_{ref}, with $f_{\mathrm{aniso}} \equiv 1$ at $r_d = 1.0$. It coincides with the value obtained at $Re_b = 5600$, which is a direct consequence of the strain topology being a kinematic property of the separating shear layer rather than a function of the turbulence intensity. The correction therefore reduces the modelled SGS viscosity in the shear-dominated recirculation region by a similar amount at both Reynolds numbers, providing the mechanism behind the comparable lengthening of the separation bubble reported below.

3.4.4 Profiles

The sampled profiles in Figs. 16–17 show the same streamwise development as case B: a reversed-flow zone behind the crest that recovers to a positive near-wall velocity by $x/h = 8$, and a pronounced turbulence-intensity peak in the separating shear layer that decays and broadens downstream. The absolute turbulence intensities are smaller at $Re_b = 10600$ than at $Re_b = 5600$. Because the higher Reynolds number raises the

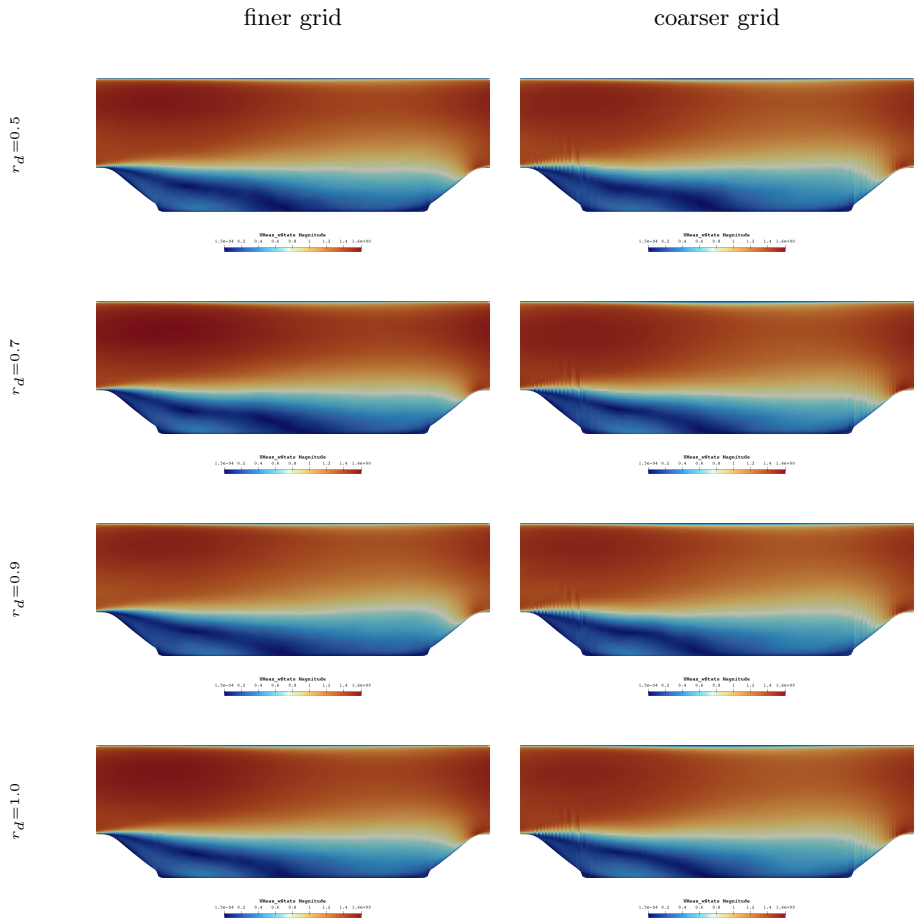


Fig. 14 Time-averaged streamwise velocity in the periodic-hills case at $Re_b = 10600$ on the finer (left column) and coarser (right column) grids at each r_d

resolved small-scale content and sharpens the mean shear, a larger fraction of the total fluctuation is carried by the resolved field, so that the relative contribution of the modelled SGS dissipation — and hence the magnitude of the r_d-induced modulation — is correspondingly smaller. This is consistent with the observation that the modelled eddy-viscosity field is more confined to the separating shear layer at the higher Reynolds number.

The response persists at both Reynolds numbers. In the smooth region ($x/h \geq 4$, $y/h \approx 1.5$–2.5) the resolved fluctuation is smallest at $r_d = 0.7$ at both Reynolds numbers: at $x/h = 8$ the values are 0.2294, 0.2172, 0.2488, and 0.2191 for $r_d = 0.5$, 0.7, 0.9, and 1.0 at $Re_b = 5600$, and 0.2309, 0.2201, 0.2396, and 0.2419 at $Re_b = 10600$. The minimum therefore coincides with the setting that produces the longest recirculation. The mean flow remains essentially unaffected by r_d at both Reynolds numbers, confirming that the correction acts on the modelled and resolved small-scale exchange rather than on the bulk transport.

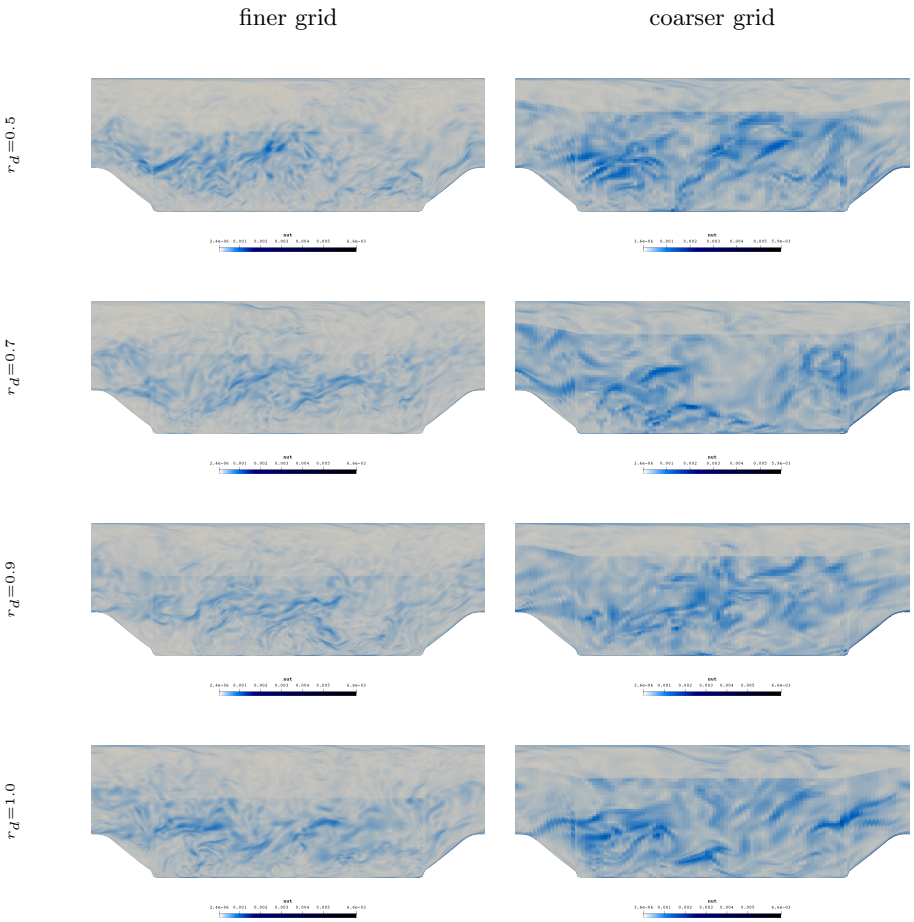


Fig. 15 SGS eddy viscosity in the periodic-hills case at $Re_b = 10600$ on the finer (left column) and coarser (right column) grids at each r_d

The quantitative effect on the separation bubble is summarised by the reattachment length, discussed below.

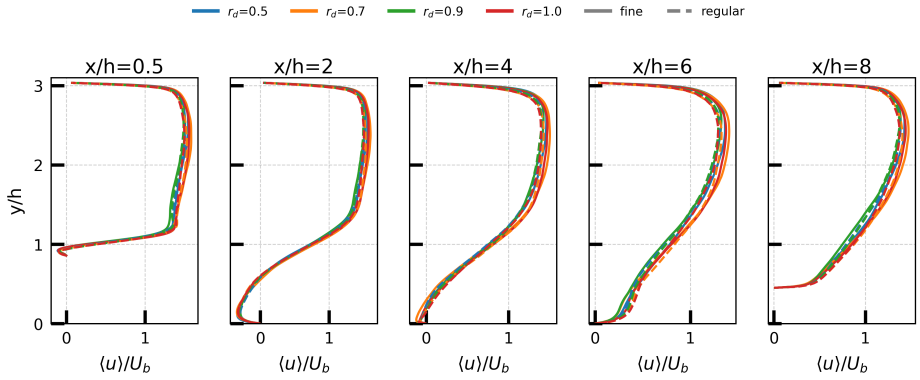


Fig. 16 Streamwise mean-velocity profiles $\langle u \rangle / U_b$ at five stations $x/h = 0.5, 2, 4, 6, 8$ for the periodic-hills case at $Re_b = 10600$ (case C) on the fine (solid) and coarser (dashed) grids at each r_d

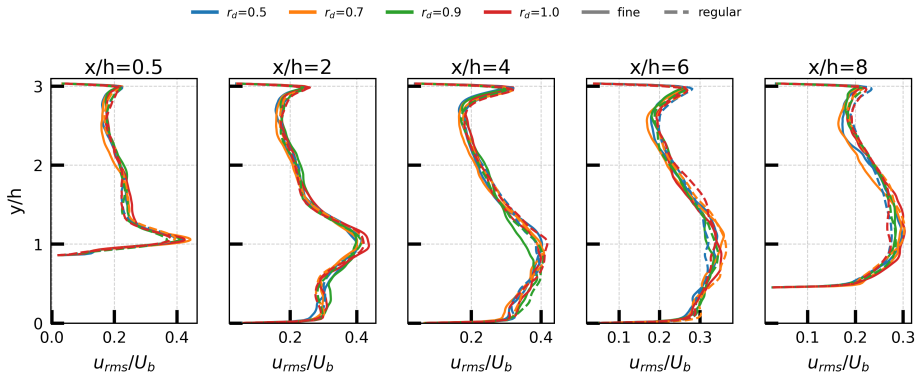


Fig. 17 Turbulence-intensity profiles u_{rms}/U_b at the same five stations for $Re_b = 10600$ (case C), fine (solid) and coarser (dashed) grids at each r_d

The reattachment length x_R/h provides a compact quantitative measure of the separation bubble. Tables 2 and 3 report the reattachment length for both Reynolds numbers and all four r_d values, next to reference data for the same configuration. At $Re_b = 5600$ the reattachment length increases from $4.83h$ at $r_d = 0.5$ to $5.19h$ at $r_d = 0.7$, then decreases to $5.14h$ at $r_d = 0.9$ and $4.91h$ at $r_d = 1.0$. The same non-monotonic response is observed at $Re_b = 10600$, reaching $5.15h$ at $r_d = 0.7$ and $4.59h$ at $r_d = 1.0$. In both cases the longest separation bubble occurs at the intermediate setting $r_d = 0.7$, and the isotropic limit $r_d = 1.0$ recovers the Smagorinsky baseline. The two Reynolds numbers give comparable values, and the longest recirculation occurs at the same setting in both, despite the different turbulence intensities, which supports the interpretation that the effect is governed by the strain topology rather than by the Reynolds number.

The isotropic limit provides the direct comparison with the reference data, because $r_d = 1.0$ reproduces the standard Smagorinsky closure. At $Re_b = 5600$ it gives $x_R/h =$

Table 2 Reattachment length x_R/h at $Re_b = 5600$ (case B) placed next to reference data for the same configuration. The reference values are those reported in the cited studies and compiled in Ref. [34]. The present values are measured as the zero crossing of the time-averaged streamwise velocity on the near-wall line $y/h = 0.001$ over the flat floor, $1.929 \leq x/h \leq 7.071$

Study	Method	x_R/h
Rapp & Manhart [32]	laser Doppler anemometry	4.83
Breuer et al. [30] (LESOCC)	LES	5.09
Breuer et al. [30] (MGLET)	DNS	5.14
Krank et al. [33]	under-resolved DNS	4.82 ± 0.09
Krank et al. [33]	DNS	5.04 ± 0.09
Prieto Saavedra et al. [34]	implicit LES	4.73
Present, $r_d = 0.5$	LES (this work)	4.83
Present, $r_d = 0.7$	LES (this work)	5.19
Present, $r_d = 0.9$	LES (this work)	5.14
Present, $r_d = 1.0$	LES (this work)	4.91

Table 3 Reattachment length x_R/h at $Re_b = 10600$ (case C) placed next to reference data for the same configuration. The reference values are those reported in the cited studies and compiled in Ref. [34]; the present values are obtained as in Table 2

Study	Method	x_R/h
Fröhlich et al. [35] (LESOCC)	LES	4.56
Fröhlich et al. [35] (STREAM)	LES	4.72
Hickel et al. [36]	implicit LES	4.30
Breuer et al. [30] (LESOCC)	LES	4.69
Krank et al. [33]	under-resolved DNS	4.57 ± 0.06
Krank et al. [33]	DNS	4.51 ± 0.06
Present, $r_d = 0.5$	LES (this work)	4.74
Present, $r_d = 0.7$	LES (this work)	5.15
Present, $r_d = 0.9$	LES (this work)	4.70
Present, $r_d = 1.0$	LES (this work)	4.59

4.91, which lies between the experimental value of Rapp et al. (4.83) and the LES and DNS benchmarks of Breuer et al. (5.09 and 5.14) and inside the spread of the under-resolved DNS and implicit LES results (4.73–5.04). At $Re_b = 10600$ the same setting gives 4.59, against 4.69 for the LES of Breuer et al. and 4.51–4.72 across the remaining reference LES and DNS studies. The spread of the published values at a given Reynolds number is about $0.4h$ in both cases, which is of the same order as the spread produced here by r_d ($0.36h$ at $Re_b = 5600$ and $0.56h$ at $Re_b = 10600$).

The reattachment lengths agree with the mechanism of Sec. 3.2. Equation (19) predicts that the modelled SGS momentum exchange across the separated shear layer is reduced monotonically as r_d decreases and that the reduction saturates, and the field data follow that ordering: the reduction $1 - \nu_t/\nu_t^{\mathrm{SM}}$ in the recirculation region is largest at $r_d = 0.5$, smaller at 0.7, smaller still at 0.9, and zero at $r_d = 1$. The measured

bubble length responds in the same direction for every $r_d < 1$, growing from $4.91h$ at the standard setting to $5.19h$ at $r_d = 0.7$, and the strongest response occurs where the weakened coupling is most effective at sustaining the recirculation. Beyond that point the correction continues to reduce ν_t, so a second effect takes over: as the coupled SGS term of Eq. (18) is driven further from the Smagorinsky level, the resolvent response of the separated layer changes sign in its net effect on the bubble, and the recirculation shortens again. The measured smooth-region fluctuation tracks this reversal rather than the magnitude of the ν_t reduction, with its minimum occurring at the same intermediate setting as the longest bubble. The balance of the two therefore places the longest recirculation at $r_d \approx 0.7$ rather than at the smallest r_d tested, and it is controlled by the single parameter $\hat{\delta}$: the recirculation can be tuned in either direction from the standard Smagorinsky setting by moving r_d away from unity.

The Reynolds-number comparison confirms that the mechanism is kinematic. Because $\langle\alpha\rangle$ is a property of the separating shear layer (Eq. (17)), the topology indicator takes essentially the same value at $Re_b = 5600$ and 10600, and the longest recirculation occurs at the same r_d in both cases. The absolute values are shorter at the higher Reynolds number, as expected for a thinner separating shear layer. The topology indicator thus sets the *location of the longest recirculation* and the Reynolds number the *magnitude*, and the two effects separate cleanly.

4 Conclusions

A relaxation-rate-separated Smagorinsky model has been developed. It reactivates a degree of freedom latent in the D3Q27 multiple- relaxation-time (MRT) operator—the independent control of the diagonal and off-diagonal relaxation rates—and condenses it into a single ratio $r_d = s_{\mathrm{diag}}/s_{\mathrm{off}}$. Through an algebraic correction factor $f_{\mathrm{aniso}}(\alpha; r_d)$, this separation is mapped onto an eddy viscosity modulated by the local strain-rate topology, so that the model retains the simplicity of the Smagorinsky closure while introducing a direction-dependent response. The model was validated on a plane jet and against reference data for periodic hills at two Reynolds numbers. The main findings are:

The analysis of the preceding section identifies the term through which the correction enters the flow, and that term governs every effect reported above. Substituting the first-order expansion Eq. (14) into the filtered momentum balance shows that the correction acts on the momentum flux through the product of the strain gradient and the topology gradient, Eq. (16). Three properties follow directly from that expression, and each is confirmed by the measurements.

- *The correction is graded by the local strain topology and thins the shear layer in which it acts.* The added momentum-flux term is proportional to $\partial_j \alpha \, \partial_j \langle u \rangle$, and in the plane jet the α distribution is bimodal with weight at both extremes, so the two populations of cells receive different modulation strengths and the response of the jet is set by their relative weight. The measured f_{aniso} is smallest in the shear-layer decile and largest in the quiescent free stream, so the correction removes the greatest amount of modelled dissipation exactly where the SGS stress drives the layer. The consequence is a thinner and longer-lived shear layer: the vorticity thickness at $x/d = 8$ on the fine grid is $0.405d$ at $r_d = 0.5$ against $0.625d$ at $r_d = 1.0$, and the time-averaged centerline velocity at $x/d = 12$ is correspondingly higher, 0.930 against 0.706. The reduced cross-layer momentum exchange therefore leaves the resolved motion concentrated in a thinner band, which is what the instantaneous fields show: the two shear layers remain identifiable further downstream and break down into finer structures than under the standard closure.
- *The separated shear layer defines the response, and the magnitude follows from the strain tensor alone.* In the recirculation region the resolved strain-rate tensor collapses to a single off-diagonal component (Eq. (17)), so the sensor settles at the shear end of its range below α_{ref}, identically at both Reynolds numbers. The measured eddy viscosity in that region falls below the Smagorinsky value for every $r_d < 1$, vanishes at $r_d = 1$, and decreases monotonically as r_d departs from unity, following the ordering of Eq. (19). Because the sensor value is fixed by the geometry of the separation, both the sign and the approximate magnitude of the correction in a separated shear layer are known from the mean flow before the simulation is run.
- *Weakening the SGS coupling lengthens the recirculation, and quiets the smooth region above it.* The SGS momentum exchange across the layer scales as $\nu_t U_s/\delta_s$, so the reduction above thins the coupling between the recirculation zone and the free stream and delays the entrainment that closes the bubble. The measured reattachment length grows from $4.91h$ at $r_d = 1.0$ to $5.19h$ at $r_d = 0.7$ at $Re_b = 5600$, and

from $4.59h$ to $5.15h$ at $Re_b = 10600$, and the resolved turbulence intensity in the smooth region above the recirculation zone is lowest at the same setting, $r_d = 0.7$. The two Reynolds numbers give the same behaviour, which follows from $\langle\alpha\rangle$ being set by the geometry, and the response saturates as r_d decreases because the bracket of Eq. (18) saturates. This is why the longest bubble occurs at an intermediate value near $r_d = 0.7$: beyond that point the coupled SGS term of Eq. (18) is driven far enough from the Smagorinsky level that the resolvent response of the separated layer reverses, and the recirculation shortens again. The correction therefore operates through a mechanism that continues to act at r_d values well below unity, in the same way as the standard closure it modulates.

The correction is thus a topology-selective operator rather than a dissipation knob. Its strength in a given region is read directly from the local strain-rate tensor through α, so the same setting of r_d produces a strong response in a separated or impinging shear layer and a weak one where the strain field is topologically uniform; across the wall-bounded flows examined here, values near $r_d = 0.7$ give the longest recirculation zone and the highest resolved turbulence intensity, so that a single value of r_d sets both. Since the correction enters the momentum balance through $\nabla\alpha$, a local dynamic procedure that sets r_d from the resolved topology itself is a natural extension. The formulation is developed here for the D3Q27 set; extension to other MRT sets and to strong heat transfer and high-Mach-number compressibility follows the same construction.

Acknowledgements. The high-performance computing resources provided by the National Supercomputing Center of Tianjin are gratefully acknowledged. This work was supported by the National Natural Science Foundation of China (No. 22508146).

Declarations

- **Funding:** This work was supported by the National Natural Science Foundation of China (No. 22508146). The high-performance computing resources provided by the National Supercomputing Center of Tianjin are gratefully acknowledged.
- **Competing interests:** The authors have no relevant financial or non-financial interests to disclose.
- **Ethics approval:** Not applicable.
- **Consent to participate:** Not applicable.
- **Consent for publication:** Not applicable.
- **Data availability:** The data that support the findings of this study are available from the corresponding author upon reasonable request.
- **Materials availability:** Not applicable.
- **Code availability:** The code that supports the findings of this study is available from the corresponding author upon reasonable request.
- **Author contribution:**

References

[1] Smagorinsky, J.: General circulation experiments with the primitive equations: I.

the basic experiment. Mon. Weather Rev. **91**(3), 99–164 (1963)

[2] Sagaut, P.: Large Eddy Simulation for Incompressible Flows, 2nd edn. Springer, Berlin (2002)

[3] Pope, S.B.: Turbulent Flows. Cambridge University Press, Cambridge (2000)

[4] Trias, F.X., Gorobets, A., Silvis, M.H., Verstappen, R.W.C.P., Oliva, A.: A new subgrid characteristic length for turbulence simulations on anisotropic grids. Phys. Fluids **29**, 115109 (2017)

[5] Oberle, D., Pruett, C.D., Jenny, P.: Temporal large-eddy simulation based on direct deconvolution. Phys. Fluids **32**, 065112 (2020)

[6] Shao, L., Zhang, Z.S., Cui, G.X., Xu, C.X.: Subgrid modeling of anisotropic rotating homogeneous turbulence. Phys. Fluids **17**, 115106 (2005)

[7] Cui, G.X., Xu, C.X., Fang, L., Shao, L., Zhang, Z.S.: A new subgrid eddy-viscosity model for large-eddy simulation of anisotropic turbulence. J. Fluid Mech. **582**, 377–397 (2007)

[8] Cimarelli, A., De Angelis, E.: Anisotropic dynamics and sub-grid energy transfer in wall-turbulence. Phys. Fluids **24**, 015102 (2012)

[9] Manzanero, J., Ferrer, E., Rubio, G., Valero, E.: Design of a Smagorinsky spectral vanishing viscosity turbulence model for discontinuous Galerkin methods. Comput. Fluids **200**, 104440 (2020) https://doi.org/10.1016/j.compfluid.2020.104440

[10] Zeng, K., Li, Z., Rana, Z.A., Jenkins, K.W.: Implicit large eddy simulations of turbulent flow around a square cylinder at Re = 22,000. Comput. Fluids **226**, 105000 (2021) https://doi.org/10.1016/j.compfluid.2021.105000

[11] Posa, A., Broglia, R.: Characterization of the turbulent wake of an axial-flow hydrokinetic turbine via large-eddy simulation. Comput. Fluids **216**, 104815 (2021) https://doi.org/10.1016/j.compfluid.2020.104815

[12] Shen, J., Chen, X., Fu, L.: Development and assessment of an improved Baldwin–Lomax turbulence model for complex hypersonic flows in two and three dimensions. Comput. Fluids **305**, 106917 (2026) https://doi.org/10.1016/j.compfluid.2025.106917

[13] Lallemand, P., Luo, L.-S.: Theory of the lattice Boltzmann method: Dispersion, dissipation, isotropy, Galilean invariance, and stability. Phys. Rev. E **61**(6), 6546–6562 (2000)

[14] d'Humieres, D., Ginzburg, I., Krafczyk, M., Lallemand, P., Luo, L.-S.: Multiple-relaxation-time lattice Boltzmann models in three dimensions. Philos. Trans. R.

Soc. A **360**(1792), 437–451 (2002)

[15] Suga, K., Kuwata, Y., Takashima, K., Chikasue, R.: A D3Q27 multiple-relaxation-time lattice Boltzmann method for turbulent flows. Comput. Math. Appl. **69**(6), 518–529 (2015)

[16] Simonis, S., Oberle, D., Gaedtke, M., Jenny, P., Krause, M.J.: Temporal large eddy simulation with lattice Boltzmann methods. J. Comput. Phys. **454**, 110991 (2022)

[17] Batchelor, G.K.: The Theory of Homogeneous Turbulence. Cambridge University Press, Cambridge (1953)

[18] Germano, M., Piomelli, U., Moin, P., Cabot, W.H.: A dynamic subgrid-scale eddy viscosity model. Phys. Fluids A **3**(7), 1760–1765 (1991)

[19] Nicoud, F., Ducros, F.: Subgrid-scale stress modelling based on the square of the velocity gradient tensor. Flow Turbul. Combust. **62**(3), 183–200 (1999)

[20] Vreman, A.W.: An eddy-viscosity subgrid-scale model for turbulent shear flow: Algebraic theory and applications. Phys. Fluids **16**(10), 3670–3681 (2004)

[21] Rozema, W., Bae, H.J., Moin, P., Verstappen, R.: Minimum-dissipation models for large-eddy simulation. Phys. Fluids **27**, 085107 (2015)

[22] Verstappen, R.W.C.P.: How much eddy dissipation is needed to counterbalance the nonlinear production of small, unresolved scales in a large-eddy simulation of turbulence? Comput. Fluids **176**, 276–284 (2018)

[23] Cimarelli, A., De Angelis, E.: The physics of energy transfer toward improved subgrid-scale models. Phys. Fluids **26**, 055103 (2014)

[24] Balan, A., Woopen, M., May, G.: Adjoint-based hp-adaptivity on anisotropic meshes for high-order compressible flow simulations. Comput. Fluids **139**, 47–67 (2016) https://doi.org/10.1016/j.compfluid.2016.03.029

[25] Hassan, W., Picasso, M.: An anisotropic adaptive finite element algorithm for transonic viscous flows around a wing. Comput. Fluids **111**, 33–45 (2015) https://doi.org/10.1016/j.compfluid.2015.01.002

[26] Sun, Y., Qi, H., Zhang, G., Wu, Y.: A novel dynamic subgrid-scale model based on partial-averaged velocity for large eddy simulation. Phys. Fluids **36**, 025114 (2024) https://doi.org/10.1063/5.0183372

[27] Le Ribault, C., Sarkar, S., Stanley, S.: Large eddy simulation of a plane jet. Phys. Fluids **11**(10), 3069–3083 (1999)

[28] Stanley, S., Sarkar, S., Mellado, J.: A study of the flow-field evolution and mixing

in a planar turbulent jet using direct numerical simulation. J. Fluid Mech. **450**, 377–407 (2002)

[29] Thomas, F., Chu, H.: An experimental investigation of the transition of a planar jet: Subharmonic suppression and upstream feedback. Phys. Fluids A **1**(9), 1566–1587 (1989)

[30] Breuer, M., Peller, N., Rapp, C., Manhart, M.: Flow over periodic hills A Numerical and Experimental study in a wide range of Reynolds numbers. Comput. Fluids **38**(2), 433–457 (2009)

[31] Manceau, R., et al.: Summary of the ERCOFTAC Case Conference on Periodic Hills. ERCOFTAC Bulletin (2011). ERCOFTAC classic collection

[32] Rapp, C., Manhart, M.: Flow over periodic hills: an experimental study. Exp. Fluids **51**, 247–269 (2011) https://doi.org/10.1007/s00348-011-1045-y

[33] Krank, B., Kronbichler, M., Wall, W.A.: Direct numerical simulation of flow over periodic hills up to $Re_H = 10{,}595$. Flow Turbul. Combust. **101**, 521–551 (2018) https://doi.org/10.1007/s10494-018-9941-3

[34] Prieto Saavedra, L., Radburn, C.E.N., Collard-Daigneault, A., Blais, B.: An implicit large-eddy simulation perspective on the flow over periodic hills. Comput. Fluids **283**, 106390 (2024) https://doi.org/10.1016/j.compfluid.2024.106390

[35] Fröhlich, J., Mellen, C.P., Rodi, W., Temmerman, L., Leschziner, M.A.: Highly resolved large-eddy simulation of separated flow in a channel with streamwise periodic constrictions. J. Fluid Mech. **526**, 19–66 (2005) https://doi.org/10.1017/S0022112004002812

[36] Hickel, S., Kempe, T., Adams, N.A.: Implicit large-eddy simulation applied to turbulent channel flow with periodic constrictions. Theor. Comput. Fluid Dyn. **22**, 227–242 (2008) https://doi.org/10.1007/s00162-007-0069-7